PCCP

PAPER

Cite this: *Phys. Chem. Chem. Phys.*, 2018, **20**, 17448

First-principles description of oxygen self-diffusion in rutile TiO_2: assessment of uncertainties due to enthalpy and entropy contributions†

Heonjae Jeong,[a] Edmund G. Seebauer[b] and Elif Ertekin*[a]

Received 30th April 2018,
Accepted 8th June 2018

DOI: 10.1039/c8cp02741b

rsc.li/pccp

Properties related to transport such as self-diffusion coefficients are relevant to fuel cells, electrolysis cells, and chemical/gas sensors. Prediction of self-diffusion coefficients from first-principles involves precise determination of both enthalpy and entropy contributions for point defect formation and migration. We use first-principles density functional theory to estimate the self-diffusion coefficient for neutral O_i^0 and doubly ionized O_i^{2-} interstitial oxygen in rutile TiO_2 and compare the results to prior isotope diffusion experiments. In addition to formation and migration energy, detailed estimates of formation and migration entropy incorporating both vibrational and ionization components are included. Distinct migration pathways, both based on an interstitialcy mechanism, are identified for O_i^0 and O_i^{2-}. These result in self-diffusion coefficients that differ by several orders of magnitude, sufficient to resolve the charge state of the diffusing species to be O_i^{2-} in experiment. The main sources of error when comparing computed parameters to those obtained from experiment are considered, demonstrating that uncertainties due to computed defect formation and migration entropies are comparable in magnitude to those due to computed defect formation and migration energies. Even so, the composite uncertainty seems to limit the accuracy of first-principles calculations to within a factor of $\pm 10^3$, demonstrating that direct connections between computation and experiment are now increasingly possible.

1. Introduction

Mechanistic interpretation of self-diffusion measurements in semiconductors often suffers from questions about the specific microscopic mechanisms to which the experimental measurements respond as well as limitations intrinsic to first-principles calculation methods. On the experimental side, the identities of the key mobile species can be difficult to ascertain and vary with the availability of kinetic pathways capable of creating the species that are most favorable energetically. On the first-principles side, limitations of density functional theory (DFT) pertain to energetic parameters such as thermodynamic enthalpies and kinetic activation barriers, and even more to the corresponding entropies and pre-exponential factors. However, the use of nearby surfaces to provide facile defect creation pathways that permit closer approach to thermodynamic equilibrium,[1–3] together with key improvements to DFT techniques,[4] make direct quantitative connection between diffusion measurements and computations increasingly reliable. The present work employs DFT calculations and detailed entropy estimates to make such a connection for the case of oxygen self-diffusion in rutile TiO_2.

Dependence of rutile's physical and electronic properties upon oxygen defects has been discussed in relation to applications in catalysis,[5–7] photocatalysis[8] and oxygen storage.[9] The majority O-related point defect observed under many conditions is the O vacancy (V_O),[10,11] although DFT calculations suggested[12,13] that the O interstitial (O_i) is thermodynamically more stable. Atomically clean surfaces provide a kinetically necessary pathway for O_i to supplant V_O as the majority.[2,14] Prior experiments demonstrating this latter phenomenon employed isotopic exchange experiments with single crystals, with corresponding isotopic diffusion profiles measured over a distance of many nanometers with secondary ion mass spectrometry (SIMS). Modeling by analytical[14] and microkinetic[15,16] techniques provided estimates of activation energies and pre-exponential factors the effective diffusivities over this length scale, as well as site-hopping diffusivities for O_i. However, direct atomic scale insights into the diffusion mechanism are lacking. From DFT, only activation energies for site hopping

[a] *Department of Mechanical Science and Engineering, University of Illinois at Urbana-Champaign, Urbana, Illinois 61801, USA. E-mail: ertekin@illinois.edu*
[b] *Department of Chemical and Biomolecular Engineering, University of Illinois at Urbana-Champaign, Urbana, Illinois 61801, USA*

† Electronic supplementary information (ESI) available. See DOI: 10.1039/c8cp02741b

exist in the literature,[17,18] with the estimates being widely disparate.

The present DFT calculations help to resolve those differences, and provide thermodynamic and rate parameters that agree remarkably well with the experiments. Differences in the stable configuration of neutral O_i and ionized O_i^{2-} oxygen interstitials are identified, and unique migration mechanisms are found for each. These differences give rise to calculated self-diffusion coefficients that differ by several orders of magnitude for O_i^0 and O_i^{2-}, large enough to resolve the charge state of the diffusing species in experiment. Detailed estimates of formation and migration entropy incorporating both vibrational and ionization components indicate that entropic contributions to the motion are mild in this case. The computational determination ΔS_{form} and ΔS_{mig} has not been commonly practiced, partly because estimation of useful accuracy requires extensive resources of hardware that have become available only in recent years. The analysis presented demonstrates the linking of the experimentally obtained parameters to atomic-scale mechanisms, reveals the mobile species is most likely O_i in the 2− ionized charge state as previously surmised, and highlights the main sources of uncertainty that arise when making such comparisons. It is estimated self-diffusion coefficients can be determined from first-principles to within approximately three orders of magnitude of experiment, suggesting that such comparisons are now in reach.

2. Methods

The experimental tracer coefficients that served as the basis for comparison were measured over a length scale of many atomic diameters, and therefore contain kinetic parameters pertaining to both formation and migration. At chemical equilibrium, the formation parameters incorporate both energies and enthalpies. The migration parameters are often formulated in an analogous way, meaning that most complete forms of comparison between experimental and computational diffusivities require computed entropies as well as energies. Neglect of entropies in this context can lead to very large errors involving several orders of magnitude in some semiconductors, as was shown in the 1970s and 80s.[19–22]

2.A. Formulation of tracer diffusion coefficient

The tracer atom diffusion coefficient (D^*) under thermodynamic equilibrium is given by[23,24]

$$D^* = fZcD, \tag{1}$$

where c denotes the concentration of the diffusing defect, and D the hopping diffusivity. The parameter $f = 1 - \frac{1}{Z}$ is the correlation factor, and Z is the coordination number. For O_i in rutile, $Z = 3$.

The hopping diffusivity incorporates a summation over all possible migration paths i and defect types d according to

$$D = \frac{1}{6}\sum_i \xi_i \Gamma_i^{\mathrm{d}} \left|\vec{\lambda}_i\right|^2, \tag{2}$$

where ξ_i is the number of symmetry-equivalent sites available for path i and $\vec{\lambda}_i$ is the jump vector between the initial and final configurations. For O_i in both charge states, $\xi = 8$. To obtain the diffusion coefficient $D_{\hat{z}}{}^*$ along direction $\hat{z}$, the projection of the jump vector $\vec{\lambda}_i$ is utilized in eqn (2). The rate Γ_i^{d} at which the defect jumps *via* path i obeys an Arrhenius form

$$\Gamma_i^{\mathrm{d}} = \Gamma_{\mathrm{o},i} \exp\left(-\frac{\Delta G_{\mathrm{mig},i}}{k_{\mathrm{B}}T}\right), \tag{3}$$

where $\Gamma_{\mathrm{o},i}$ denotes the attempt frequency, k_{B} the Boltzmann constant, T the temperature. The Gibbs free energy of migration is

$$\Delta G_{\mathrm{mig},i} = \Delta E_{\mathrm{mig},i} - T\Delta S_{\mathrm{mig},i} + P\Delta V_{\mathrm{mig},i}, \tag{4}$$

where $\Delta E_{\mathrm{mig},i}$ is the migration internal energy, $\Delta S_{\mathrm{mig},i}$ is the migration entropy, and $\Delta V_{\mathrm{mig},i}$ is the migration volume change. Formally these quantities represent respectively the difference in internal energy, entropy, and volume between the defect at the transition state and in the metastable configuration. For O_i we employed $\Gamma_{\mathrm{o}} = 1 \times 10^{13}\ \mathrm{s}^{-1}$.

The concentration presents a standard Boltzmann factor given by

$$c = \exp\left(-\frac{\Delta G_{\mathrm{form}}}{k_{\mathrm{B}}T}\right), \tag{5}$$

where

$$\Delta G_{\mathrm{form}} = \Delta E_{\mathrm{form}} - T\Delta S_{\mathrm{form}} + P\Delta V_{\mathrm{form}} \tag{6}$$

denotes the Gibbs free energy of defect formation, and ΔE_{form}, ΔS_{form}, and ΔV_{form} are the change in internal energy, entropy, and volume upon formation of the defect. Given typical values for ΔV_{form}, pressures on the order of 1 kbar are needed for activation volume effects to become significant and can be neglected here.[25,26]

Upon aggregation of all these definitions, D^* for O_i becomes

$$D^* = \frac{1}{6} f Z \xi \Gamma_{\mathrm{o}} \left|\vec{\lambda}_i\right|^2 \exp\left(\frac{\Delta S_{\mathrm{form}} + \Delta S_{\mathrm{mig}}}{k_{\mathrm{B}}}\right) \exp\left(-\frac{\Delta E_{\mathrm{form}} + \Delta E_{\mathrm{mig}}}{k_{\mathrm{B}}T}\right). \tag{7}$$

2.B. Computation of energies and structures

Our DFT calculations[27,28] employ the Vienna *Ab Initio* Software Package (VASP)[29,30] together with projector augmented wave (PAW)[31] and the Perdew–Burke–Eznerhof (PBE)[32] generalized gradient approximation (GGA) for the exchange–correlation functional. The plane-wave energy cutoff was set to 520 eV. For bulk rutile, we obtain lattice constants of a = 4.652 Å, c = 2.970 Å, and internal parameter u = 0.305 Å, in good agreement with calculated values from the previous DFT-GGA results, which were a = 4.649, c = 2.972, and u = 0.304,[33,34] compared to experimental values of a = 4.690, c = 2.990, and u = 0.305.[35] To simulate defects, we used 3 × 3 × 4 TiO_2 supercells containing 216 atoms together with 2 × 2 × 2 Monkhorst–Pack k-point sampling of the Brillouin zone. The internal ion coordinates were relaxed until the residual forces

on each ion were smaller than 0.01 eV Å^{-1}. The climbing image nudged elastic band (CI-NEB) method[36] was employed to estimate O_i migration energy barriers ΔE_{mig} along the minimum energy pathway (MEP) with spring constants set to −5 eV Å^{-1} and the criterion for atomic geometry relaxation loosened to 0.03 eV Å^{-1}.

The internal energy of defect formation ΔE_{form} was determined *via* the usual formulation[37]

$$\Delta E_{form} = \left(E_{(TiO_2+O_i)} - E_{(TiO_2)}\right) - \mu_O + q(E_V + E_F). \quad (8)$$

Here $E_{(TiO_2+O_i)}$ and $E_{(TiO_2)}$ respectively denote the DFT-computed total energy of the supercell containing the oxygen interstitial and of the perfect supercell, μ_O is the oxygen chemical potential, and E_F is the Fermi level relative to the valence band maximum (VBM) E_V ($0 < E_F < E_g$), where E_g is the experimental band gap. Results are shown for the oxygen rich environment corresponding to the experimental point of comparison (T = 700 °C and $P_{O_2} = 10^{-5}$ Torr).[2] The chemical potential $\mu_i = \mu_i^0 + \Delta\mu_i$, where μ_i^0 is the chemical potential of the atomic species in the standard condition, $\Delta\mu_i$ represents the temperature and pressure variance, and $\Delta\mu_O = -0.23$ eV per atom for oxygen and $\Delta\mu_{Ti} = -9.27$ eV per atom for titanium (see ESI†). For simulation of the doubly ionized O_i^{2-} state, two extra electrons were added to the simulated DFT supercell, which are compensated by the incorporation of a homogeneous background charge.[38] Finite size effects arising from electrostatic interactions between periodic images of the charged defects are estimated using supercell extrapolation.

For the ionized defect, ΔE_{form} depends on E_F within the band gap. For direct comparison with experiment, both E_F and E_g must be estimated at the relevant temperature of roughly 700 °C. Although the literature agrees upon a linear functional form for the temperature dependence of E_g, the associated parameters vary.[39–46] To arrive at ''best'' values of those parameters, we employed maximum-likelihood (ML) estimation[47,48] to arrive at a value of E_g = 2.42 eV at T = 700 °C (see ESI†). The position of E_F was assumed to scale with the concentration of donor Ti interstitial atoms, and depends upon the effective mass of the electron, whose value has been measured numerous times[49–58] with widely disparate results. We again employed ML estimation to arrive at an effective mass of $(8.44 \pm 1.00)m_e^*$ (see ESI†). The concentration of Ti interstitials depends upon both temperature and the partial pressure of O_2, and can be estimated with a defect disorder model appropriate for this experimental system. We employed a model developed specifically for these conditions,[16] using $P_{O_2} = 10^{-5}$ Torr. These computations ultimately yielded $E_F = 1.58 \pm 0.003$ eV.

2.C. Computation of entropies

The relevant entropies contain several contributions that originate from vibrational and configurational sources, and in semiconductors, from ionization.[19] We neglected configurational contributions, which are usually small compared to the others.[59,60]

The ionization entropy arises from changes in the vibrational spectrum in response to the defect's ionization by releasing one or more electrons or holes to wander freely in the bands.[19] This release puts carriers into or removes carriers from antibonding orbitals of the solid, and can slightly soften or harden the vibrational modes respectively. This results in a change in the magnitude of the vibrational frequencies, particularly for the local vibrational modes associated with the defect. For an initially neutral interstitial atom whose releasable carriers are spatially delocalized in the bound state, that carrier exerts roughly the same mode-softening effects in the bound state as in the free state after donation to a band. Thus, the ionization entropy lies near zero because the lattice senses little difference in softening from initial to final state. However, if the bound carriers remain localized near the ion core, they partly screen the ion core's effect on lattice vibrations. The ionization entropy then differs from zero and is commonly positive. Fortunately, DFT calculations of the vibrational spectrum already incorporate such effects implicitly, as entropic contributions from ionization come from localized changes in the vibrational spectrum. If desired, contributions of ionization to the formation or migration entropy may be identified by comparing results for the neutral and ionized states.

The vibrational entropy arises from the change in the solid's vibrational modes in response to the defect itself (formation) or its hopping transition state (migration). Both changes may involve progressive activation of increasing numbers of vibrational modes as the temperature increases, meaning that ΔS_{form} and ΔS_{mig} can exhibit a temperature dependence. The T = 0 K phonon frequencies were calculated using DFT and the finite difference method of Phonopy software.[61] Force constant calculations were performed for perfect and defect-containing supercells for supercells containing 48, 72, and 216 atoms to assess finite size effects (FSEs). Once the T = 0 K mode frequencies were determined, the vibrational entropy of a supercell containing N atoms at finite non-zero temperature was estimated *via* the full harmonic approximation,[62]

$$S_{vib} = k_B \sum_{i=1}^{3N} \frac{\hbar w_i}{k_B T}\left(e^{\frac{\hbar w_i}{k_B T}} - 1\right)^{-1} - \ln\left(1 - e^{-\frac{\hbar w_i}{k_B T}}\right), \quad (9)$$

where $\hbar$ is Planck's constant, and w_i are the eigenfrequencies associated with the phonon vibrations in the crystal lattice.

The vibrational entropy of formation $\Delta S_{form}^{vib} = S_{TiO_2+O_i}^{vib} - \left(S_{TiO_2}^{vib} + S_O\right)$ was computed as the entropy difference between the defective TiO_2 supercell ($S_{TiO_2+O_i}$) and the perfect TiO_2 supercell (S_{TiO_2}) with an additional term (S_O) that accounts for the extra oxygen in the defect containing lattice. The quantity S_O is nominally the vibrational entropy per O atom in rutile TiO_2. It was obtained by distributing the total vibrational entropy per formula unit TiO_2 between Ti and O atoms according to their relative masses and presence in the crystal so that $\frac{S_{Ti}}{S_O} = \sqrt{\frac{2}{1}\frac{m_O}{m_{Ti}}} \approx 0.826$.[63] The migration entropy ΔS_{mig}^{vib} was computed as the vibrational entropy difference in the defective supercell between the transition state of a defect during a jump and the initial state.

2.D. Estimate of uncertainties in the diffusion coefficient

To assess the propagation of computational uncertainties in the various energies and entropies composing D^* into the value of D^* itself, we estimated the magnitudes of uncertainty in each of the four parameters ΔE_{form}, ΔE_{mig}, ΔS_{form}, and ΔS_{mig}. Because the two energies were computed using very similar methods, the uncertainties in ΔE_{form} and ΔE_{mig} were assumed to be correlated with each other and therefore sum together linearly. By a similar rationale, uncertainties in ΔS_{form} and ΔS_{mig} were assumed to sum linearly. However, as limiting features appeared to arise from different sources (accuracy of DFT for energies *vs.* finite size effects for entropies), the corresponding uncertainties were assumed to be uncorrelated. A sum of squares approach is therefore more appropriate to employ to describe uncertainty propagation from these constituent parameters into D^*.

Such an approach begins with eqn (7) written in nondimensional form to leave only the exponential terms on the right hand side. With the definition of the nondimensional diffusion coefficient $\mathcal{D} = 6D^* \Big/ \left(fZ\xi\Gamma_{\mathrm{o}} \left| \vec{\lambda}_i \right|^2 \right)$, the uncertainty $\sigma_{\ln \mathcal{D}}$ in $\ln(\mathcal{D})$ may be written in terms of the nondimensional energy and entropy uncertainties $\sigma_{\Delta E/k_{\mathrm{B}}T}$ and $\sigma_{\Delta S/k_{\mathrm{B}}}$ according to

$$\sigma_{\ln \mathcal{D}} = \left({\sigma_{\Delta E/k_{\mathrm{B}}T}}^2 + {\sigma_{\Delta S/k_{\mathrm{B}}}}^2 \right)^{1/2}, \qquad (10)$$

where $\Delta E = \Delta E_{\mathrm{form}} + \Delta E_{\mathrm{mig}}$ and $\Delta S = \Delta S_{\mathrm{form}} + \Delta S_{\mathrm{mig}}$. The nondimensionalization of ΔE requires the selection of a characteristic temperature. We chose 700 °C, which is within the experimental temperature range.

3. Results

Fig. 1 reports the configurations and defect formation energy for neutral (O_i^0, $q = 0$) and doubly ionized (O_i^{2-}, $q = 2-$) oxygen interstitials. The formation energy for the $q = 1-$ state previously has found to be energetically less favorable than the others under any circumstance,[12,13,64] and therefore was not considered here. Distinct from prior studies,[13] we considered possible dumbbell and split configurations in both charge states. Both configurations are metastable for both $q = 0$ and $q = 2-$ although the dumbbell is more stable for neutral O_i^0 and the split configuration for doubly ionized O_i^{2-}. The energy difference is roughly 1.8 eV in both cases.

In the neutral state, the interstitial adopts a dumbbell configuration with two symmetric Ti–O bonds (Fig. 1a). The dumbbell configuration for O_i^0 is also energetically favorable for metal oxides MgO and ZnO.[65,66] The O–O bond length is 1.45 Å, indicative of the covalent peroxide species, and is elongated compared to that in oxygen molecule (~1.24 Å). In contrast, the doubly ionized split configuration links with the nearest three Ti atoms (Fig. 1b). Fig. 1c shows the energy of defect formation ΔE_{form} as a function of E_{F}. For the most stable configurations, the ionization level $(0|2-)$ occurs at roughly $E_{\mathrm{F}} = 1$ eV above the VBM. DFT thereby confirms that the interstitials present in the experiments, for which TiO_2 is n-type, are likely to be doubly ionized.

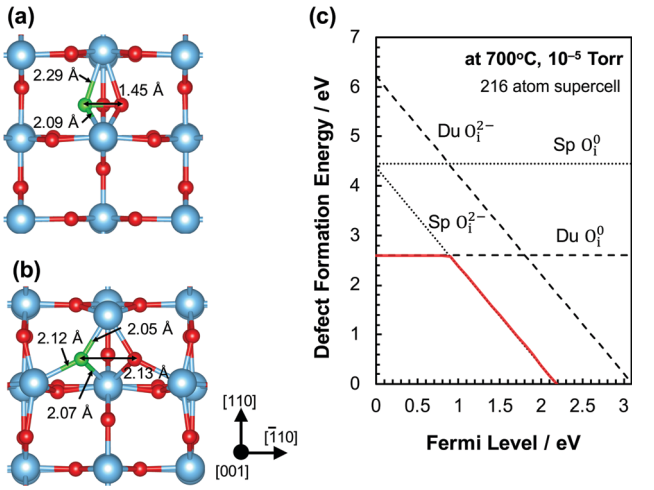

Fig. 1 Configurations of (a) neutral dumbbell O_i^0 and (b) doubly ionized split O_i^{2-} in rutile TiO_2. Titanium atoms, oxygen atoms, and oxygen interstitials are represented as blue, red, and green spheres, respectively. (c) Defect formation energy as a function of the Fermi level for O_i^0 and O_i^{2-} for prior oxygen rich experimental annealing conditions (T = 700 °C and P_{O_2} = 1.0 × 10^{-5} Torr). The red solid line presents the stable defect configuration, and Du and Sp indicate dumbbell and split configurations, respectively.

Fig. 2 shows the migration pathway and energy landscape for site-to-site hopping for neutral dumbbell O_i^0 and for ionized split O_i^{2-} along the [110] direction, since the experiments entailed injection through the (110) plane. The pathways follow an interstitialcy mechanism in which diffusion occurs *via* O_i exchange with oxygen atoms in the lattice. Such exchange has also been observed in other oxides[67] and typically exhibits a lower migration energy barrier than the direct interstitial mechanism.[68]

Fig. 2a shows that the O_i^0 dumbbell traverses a single barrier during a jump, with a migration energy barrier ΔE_{mig} of 0.59 eV. The migration of the O_i^{2-} split is more complicated, however; Fig. 2b shows the MEP traversing from a tetrahedral to a metastable octahedral state. The metastable octahedral interstitial site has also been reported elsewhere for ZnO.[24] The barrier to enter the metastable state is 0.65 eV.

The inset figures in Fig. 3 shows $\Delta S_{\mathrm{form}}^{\mathrm{vib}}$ and $\Delta S_{\mathrm{mig}}^{\mathrm{vib}}$ for O_i^0 and O_i^{2-} shown as a function of the number of atoms N in the supercell. Although the vibrational and migration entropies are negative, they become less negative as the supercell size increases. Negative values have been observed previously,[62,63] and were attributed to the artificial truncation of vibrational wavelengths imposed by finite supercell dimensions. To estimate the entropies in the dilute limit, we extrapolated to $(N \rightarrow \infty)$ at T = 700 °C using a $1/N$ scaling relation together with a weighted least squares regression approach, in which each computed value of the vibrational entropy is weighted inversely with the size of the supercell. As shown in Table 1, the extrapolated formation entropies ($\Delta S_{\mathrm{form}}^{\mathrm{vib}}$) for both the neutral and doubly ionized O_i are small, $-0.04 \pm 0.08\ k_{\mathrm{B}}$ and $0.30 \pm 0.59\ k_{\mathrm{B}}$,

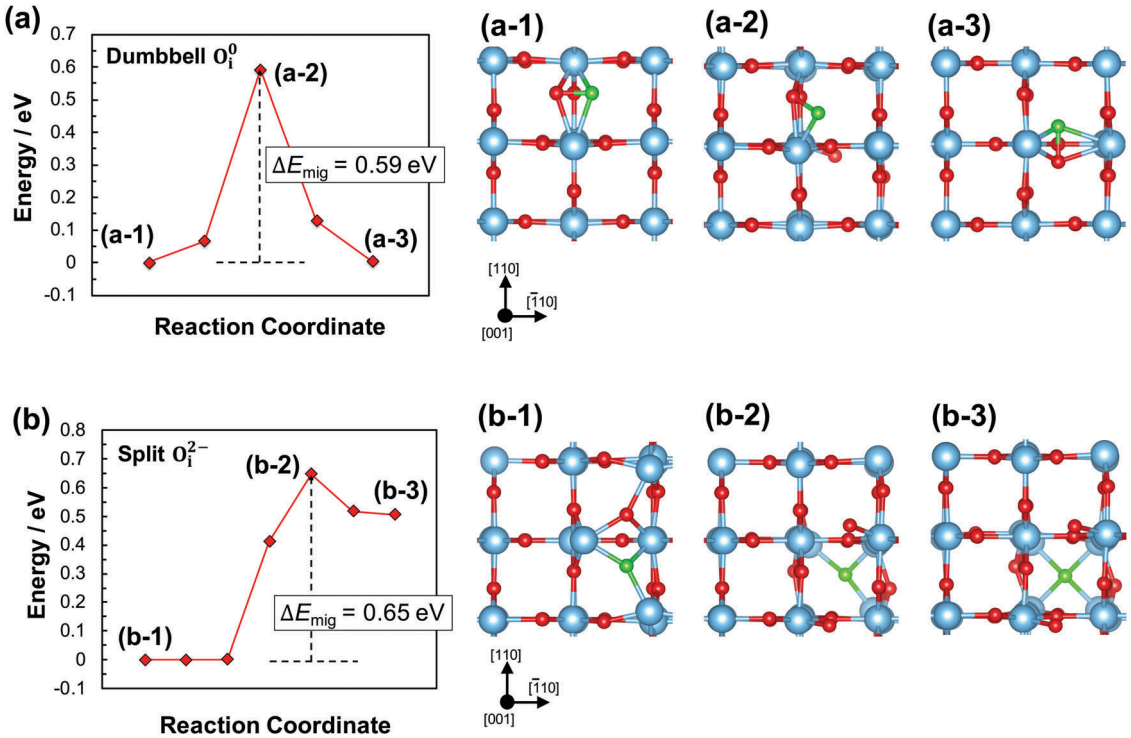

Fig. 2 Minimum energy pathway showing selected configurations for the migration of (a) dumbbell O_i^0 and (b) split O_i^{2-} in rutile TiO_2 diffusing *via* interstitialcy mechanism. The split interstitial path traverses from a tetrahedral to a metastable octahedral interstice of the rutile lattice. Titanium ions, oxygen ions, and oxygen interstitial defect are represented as blue, red, and green spheres, respectively.

respectively. The corresponding migration entropies (ΔS_{mig}^{vib}) are 0.33 ± 0.45 k_B and 0.02 ± 0.10 k_B.

4. Discussion

4.A. Comparison to experiment

Because the present work has computed both the energies and the entropies for formation and migration, it becomes possible to compare the computed values of D^* to reported experimental values obtained by both analytical[14] and microkinetic[15,16] means. Fig. 4a shows such comparisons pictorially by plotting D^* in Arrhenius form as a function of $1/k_BT$ for O_i^0 and O_i^{2-}, and Fig. 4b shows corresponding plots as a function of P_{O_2}. The first-principles values of D^* fall within two orders of magnitude of the experimental ones for the (2−) charge state. The slopes of both the temperature and pressure plots match rather closely. In contrast, the computed neutral state fall an average of four or five orders of magnitude away from the experimental ones, and the slopes are noticeably steeper for both the temperature and pressure dependence. Thus, both figures exhibit a significantly better match for the (2−) state than the neutral state; the comparison apparently can distinguish between different charge states of the diffusing species. Indeed previous experimental work[14] has already suggested the dominance of the (2−) state based on the value of the positive pressure dependence, in line with earlier first-principles computations.[69,70]

The individual energies and entropies are compared in Table 2. In view of the finding just above, the entries correspond only to the (2−) charge state. The first-principles migration energy (ΔE_{mig}) of 0.65 eV for O_i^{2-} closely matches the experimental result of (0.65 ± 0.1 eV[15,16]) derived from microkinetic analysis.

The computed entropy values for migration entropy (ΔS_{mig} = 0.02 ± 0.10 k_B) is noticeably lower than the experimental microkinetic value of 3.93 k_B. Both values may be compared with a very rough estimate provided by noting that the work done by a jumping interstitial atom may be conceptualized as a free energy of migration (ΔG_{mig}). The thermodynamic identity $\Delta S_{mig} = -\frac{\partial(\Delta G_{mig})}{\partial T}$ ref. 71 then provides an estimate of the corresponding entropy. The entropy is typically positive because the migrational work done by the moving atom against the elasticity of the lattice decreases with temperature due to lattice expansion. The rough magnitude of $\frac{\partial(\Delta G_{mig})}{\partial T}$ may be approximated by $\frac{\Delta H_{mig}}{T_m}$, where T_m is the melting temperature (~2116 K for TiO_2). The resulting migration entropy is 3.76 k_B – close to the microkinetic value but larger than the first-principles one. The first-principles estimated formation entropy (ΔS_{form} = 0.30 ± 0.59 k_B), however, is closer to the experimental value of 1.54 k_B.

4.B. Sources of uncertainty

The present work attempts the rather ambitious task of comparing first-principles kinetic parameters, not only at the level

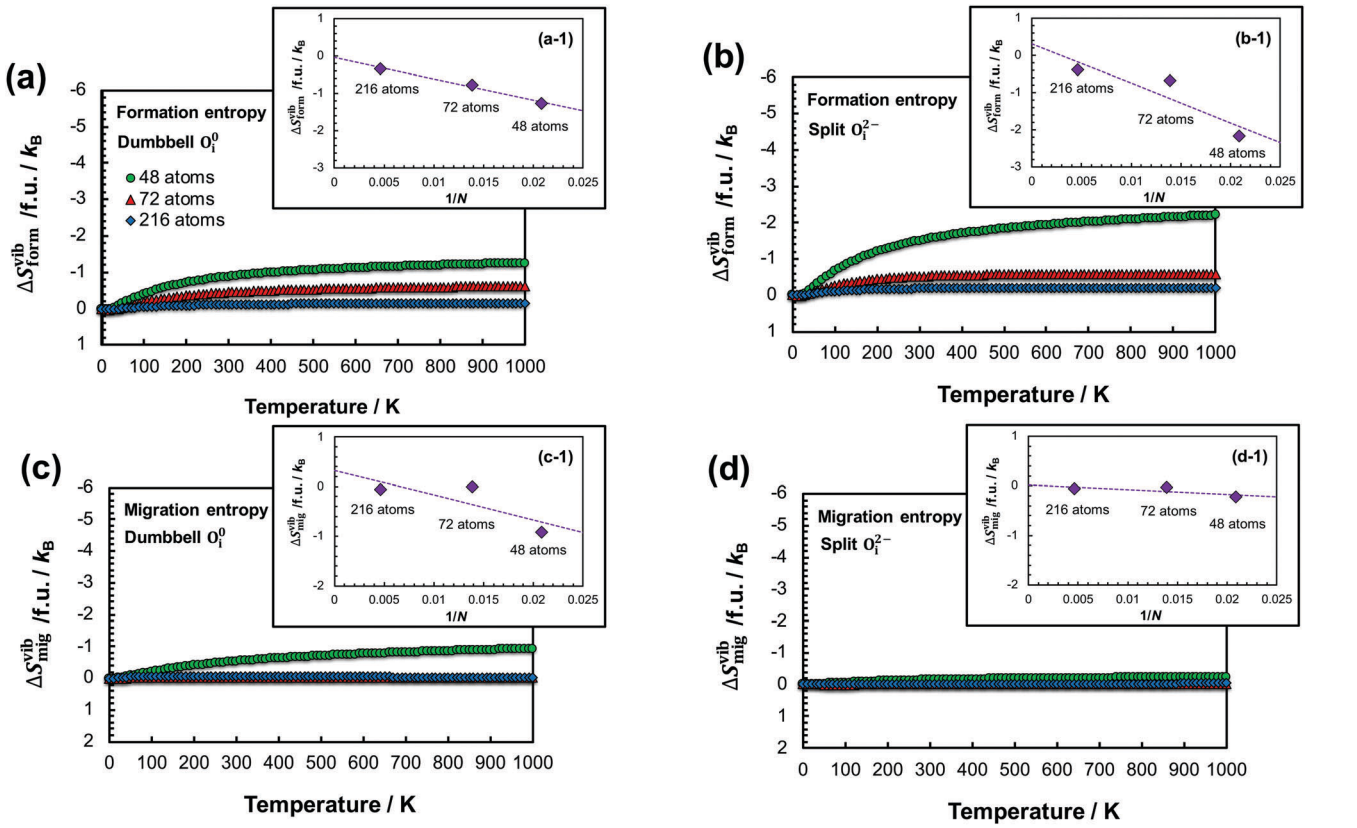

Fig. 3 Formation entropy for neutral dumbbell and negative doubly ionized split ((a) and (b)), and migration entropy for neutral dumbbell and doubly negative ionized split ((c) and (d)) for different supercell sizes (48, 72, 216 atoms). The insets show extrapolation to the thermodynamic limit ($1/N \rightarrow 0$) using a weighted least squares regression approach at T = 700 °C.

Table 1 Formation (ΔS^{vib}_{form}) and migration (ΔS^{vib}_{mig}) entropy for phonon vibration on neutral and doubly ionized negative oxygen interstitial in rutile TiO_2 at constant volume at T = 700 °C

	$\Delta S^{vib}_{form}/k_B$		$\Delta S^{vib}_{mig}/k_B$	
Supercell size/atoms	O_i^0	O_i^{2-}	O_i^0	O_i^{2-}
48	−1.25	−2.18	−0.92	−0.23
72	−0.62	−0.57	−0.01	−0.02
216	−0.15	−0.19	−0.03	−0.03
∞	−0.04(08)	0.30(59)	0.33(45)	0.02(10)

of individual energies and entropies of formation and migration, but also of those numbers aggregated into the tracer diffusion coefficient D^*. This latter comparison is important because full-blown entropy computations for diffusion have become practical only in recent years, commonly accepted benchmarks of success or systematic analyses of the possible errors do not yet exist. The computations of vibrational spectra needed for entropy estimates have a very different character from the computations of total energies that have long been commonplace for barrier heights and formation energies. Hence, it is not yet known to what extent errors in the entropy reinforce or compensate for errors in the energies. The following paragraphs provide such an analysis in the context of the errors known to be present for experimental measurements of the corresponding quantities by SIMS.

4.B.1. Computational energies. There exist several well-known uncertainties inherent in DFT calculations of point defect energetics that arise from (i) the computational engine for energy calculations (here DFT-PBE) and associated problems such as band gap underestimation, and (ii) finite size effects due to the limited supercell size particularly for ionized defects. Regarding (i), in many cases formation energies for defects can vary by several tenths of an eV between hybrid and conventional DFT.[72,73] Regarding (ii), the size of the uncertainty can be similar. The ESI† assesses the magnitude of finite size effects using supercell extrapolation and suggest that in this case it is small. In any case, for ionized defects these sources of uncertainty become somewhat moot, since the formation energy depends on the Fermi level which is also not precisely known in experiment. Even so, we estimate uncertainties in ΔE_{form} and ΔE_{mig} to be around 0.3–0.4 eV and 0.1–0.2 eV respectively. As finite size effects are largely under control in this case, these mainly arise from the selection of DFT computational engine. We estimate the uncertainty in the migration energy to be smaller than the formation energy as it is obtained as a difference between defect-containing supercells (metastable and transition state). With linear summation of the uncertainties and average values of ΔE_{form} and ΔE_{mig} taken to be 0.35 eV and 0.15 eV respectively, the composite uncertainty in ΔE equals 0.5 eV. With a characteristic temperature of 700 °C,

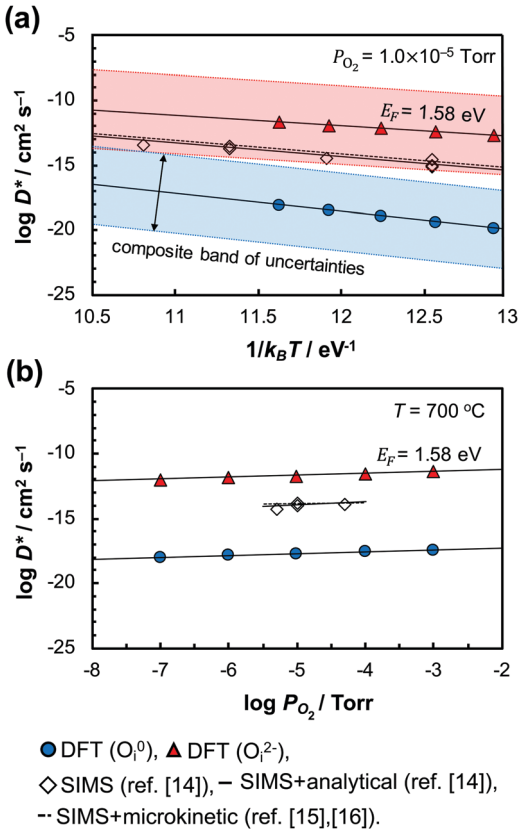

Fig. 4 Oxygen self-diffusion coefficient D^* in rutile TiO_2 from DFT calculations obtained as a function of (a) temperature at $P_{O_2} = 1.0 \times 10^{-5}$ Torr and (b) oxygen partial pressure (P_{O_2}) at T = 700 °C. Blue circles indicate O_i^0, red triangles indicate O_i^{2-}, and open diamonds indicate results from previous SIMS experiments.[14] The aggregated SIMS data were analyzed using two different approaches. Solid and dashed lines indicate analytical and microkinetic approaches,[14–16] whose results nearly overlap. For O_i^{2-}, results corresponding to a Fermi level in the semiconductor of 1.58 eV (obtained *via* maximum-likelihood estimation) are shown. In (a), the shaded area corresponds to a composite uncertainty of ±7 around the computed D^*.

Table 2 Summary of first-principles DFT results for oxygen self-diffusion *via* interstitialcy mechanism along the [110] direction in rutile TiO_2. We compare our DFT-computed quantities with those obtained by a microkinetic model from previous isotope experiments.[15,16] We present the formation energy (ΔE_{form}) estimated at the Fermi energy of 1.58 eV

Diffusion parameters	DFT calculations		SIMS experiments
	O_i^0	O_i^{2-} (E_F = 1.58 eV)	
ΔE_{form}/eV	2.60 ± 0.40	1.17 ± 0.40	0.8
ΔE_{mig}/eV	0.59 ± 0.16	0.65 ± 0.19	0.65 ± 0.1
$\Delta S_{form}/k_B$	−0.04 ± 0.08	0.30 ± 0.59	1.10 ± 0.01
$\Delta S_{mig}/k_B$	0.33 ± 0.45	0.02 ± 0.10	4.98 ± 0.36

k_BT lies near 0.1 eV, resulting in an uncertainty $\sigma_{\Delta E/k_BT}$ that is therefore about 5.

4.B.2. Computational entropies. As the computational determination ΔS_{form} and ΔS_{mig} has not been commonly practiced, there is little literature base. We surmise that the largest source of uncertainty in the calculation of entropy components arises from finite size effects. Although the supercells used here are large compared to previous efforts[22,63,74–76] on the whole they remain small. This is evident from the mostly negative entropies obtained for the finite supercells used here. The need to extrapolate to the thermodynamic limit introduces a relatively large uncertainty. Effects of anharmonicity and other considerations may also be relevant, but are not accounted for by the quasiharmonic model used here (eqn (9)). Anharmonic shifts of phonon frequencies and broadening of the phonon spectrum with changing temperature can be substantial (a few tenths of an eV per atom,[77–81] especially at high temperatures). It is not straightforward, however, to isolate the uncertainties arising from finite size effects, anharmonicity, and other considerations in the estimate of defect entropies. The uncertainties ΔS_{form} and ΔS_{mig} are probably of about equal magnitude. We estimate an aggregated uncertainty in the entropy $\sigma_{\Delta S/k_B}$ of 5, which is comparable to the uncertainty in ΔE introduced by the energy computations.

4.B.3. Experimental errors. Self-diffusion coefficients may be measured in several ways. However, the sensitivity of SIMS permits self-diffusion measurements at lower temperatures than many other methods, and more importantly enables use of the atomically clean surfaces required to generate interstitial atoms. Fundamentally, SIMS measurements yield concentration profiles. Transformation of these profiles into D^* and its constituent components requires modeling, for which there exist two primary approaches when surfaces play a major role.

One approach employs analytical solution of differential equations. This approach yields only D^* and two composite kinetic quantities (net injection flux and mean diffusion length for sequestration), but may be used with no specific defect-disorder model. The other approach involves detailed microkinetic modeling that yields both D^* and numerous thermodynamic and kinetic parameters corresponding to specific elementary steps. Yet implementation of this approach requires specific assumptions about the nature of those elementary steps and the defect disorder thermodynamics. Such assumptions often represent only educated guesses. Sequestration of O_i in TiO_2 represents an example of a mistaken guess; sequestration was originally believed to occur by kick-in to the lattice,[15] but is now known to occur in extended defects.[82] Even with an accurate sequestration model, both approaches suffer from random and systematic uncertainties, but manifest them in different ways.

Random errors arise primarily from SIMS metrology limitations that have been reviewed extensively elsewhere.[16,83] For measurements of D^* in semiconductors like TiO_2 and ZnO where the mobile interstitial atoms move many atomic diameters before sequestration, the profiles tend to be deep and wide. This shape limits the dynamic range of concentrations available in any single profile, so that SIMS errors propagate as follows.

The analytical approach method aggregates the concentration *vs.* position data profile-by-profile with all data points within each profile given the same weight in a least-squares fit. The net consequence is that concentration data with large standard deviations enter with the same weights as higher

quality data with smaller standard deviations. The resulting uncertainty in D^* ranges from $\pm 15\%$ in favorable cases to a factor of two in unfavorable ones. Error bars on the activation energies for D^* and the related composite parameters range from 0.15 to 0.35 eV.

The microkinetic approach aggregates all the concentration data at once in a single global optimization problem. Each data enters with a weighting that varies inversely with its standard deviation, meaning that higher quality data are assigned greater weight. The error bars in energy-related parameters therefore tend to be much smaller than for the analytical approach – often by a factor of two to four (*i.e.*, always below 0.1 eV). For reasons that are not yet understood, the error bars on the corresponding pre-exponential factors tend to be a bit larger, meaning that uncertainties in D^* are only somewhat smaller.

It is important to mention systematic errors originating from the unavoidable use of important simplifying assumptions. These assumptions and their limitations have been detailed elsewhere.[16,83] The analytical approach employs a deep-bulk boundary condition for the mobile species that is independent of T and P_{O_2}, and therefore tends to underestimate the T dependence compared to the microkinetic approach. However, the microkinetic global optimization procedure requires initial parameter guesses. Often there is little *a priori* basis for these guesses, leading the objective function to settle into local extrema or vary too slowly for full convergence. This effect afflicts primarily pre-exponential factors,[16] but the optimization procedure compensates by returning skewed values for the corresponding activation energies.

Importantly, such systematic uncertainties do not permit quantification in terms of conventional standard deviations, and require a more sophisticated uncertainty analysis.[84,85] The results of such an analysis depend greatly upon the details of the specific approach employed to yield diffusivities, and well as the specific experimental conditions employed. Such an analysis lies beyond the scope of this paper. However, the fitting procedures for D^* employed in both the analytical and microkinetic approaches typically compensate to a large extent the errors introduced by simplifying approximations and assumptions. Thus, the values of D^* tend to be fairly accurate for the analytical approach (a factor of two or better), although the composite parameters returned are not directly comparable to the output of DFT computations. The values of D^* from the microkinetic approach also tend to be comparably good when averaged over the entire experimental temperature range, although the temperature dependence of D^* is sometimes poorer than for the analytical approach. But the microkinetic approach yields parameters that may be compared directly with the output of DFT computations. The best mode of connection between ''experiment'' and ''first-principles computation'' is therefore a matter of judgement. In the present case of oxygen in rutile, the two experimental approaches fortunately yield results that are largely self-consistent, especially for D^*.

4.B.4. Unified uncertainty analysis. From eqn (10) and estimated uncertainties $\sigma_{\Delta E/k_BT}$ and $\sigma_{\Delta S/k_B}$ for non-dimensional energy and entropy of 5 each, the composite uncertainty is determined as $\sigma_{\ln \mathcal{D}} = \pm 7$, which corresponds to a factor of about 10^3. Because the all the factors comprising $\mathcal{D}$ other than D^* are assumed to have no error, all the uncertainty in $\mathcal{D}$ may be ascribed to D^*. The colored bands in Fig. 4a indicate the corresponding composite uncertainty in D^* computed from first principles. These bands indicate an uncertainty of about a factor of 10^3 on either side of the corresponding most-likely Arrhenius plots. The uncertainty in the experimental results of about a factor of two that is too small to depict easily on the expanded vertical scale of Fig. 4a.

The colored blue band for neutral O_i is sufficiently wide to that it does not completely exclude this pathway from consideration, especially because of some imprecision in the estimates of $\sigma_{\Delta E/k_BT}$ and $\sigma_{\Delta S/k_B}$. However, the colored bands are narrow enough to be useful in assessing the relatively likelihood of diffusional mediation by the two charge states, with the balance tipping heavily toward the $(2-)$ state.

In general, it seems that the accuracy of entropy computations by first principles have progressed to the point where they can help distinguish between diffusional mechanisms. Even though the entropic contributions to D^* are rather small for the present system, that is not the case for semiconductor diffusion in general (as mentioned in the Introduction). It is plausible to believe that entropy calculations contribute uncertainties to D^* that are comparable to those for energy. The composite uncertainty seems to limit the accuracy of first-principles calculations to a factor of within a factor of $\pm 10^3$, which should be sufficient to distinguish among diffusional species and pathways in many systems.

5. Conclusions

We use a first-principles approach to estimate self-diffusion coefficients of oxygen interstitials in rutile TiO_2, and make a direct quantitative connection to prior isotope diffusion experiments. First-principles DFT calculations of defect energies and entropies, which are aggregated to predict the self-diffusion coefficient, are presented. The presented results validate the identity of the key mobile species as negative doubly ionized O_i^{2-}, which adopts a split interstitial configuration and diffuses *via* an interstitialcy mechanism. This work highlights some of the challenges associated with making such a comparison and the main sources of uncertainty that arise due to computed energy and entropy contributions. While uncertainties due to defect formation and migration entropies remain significant, they now approach those associated with defect formation and migration energy. Even so, in general we estimate uncertainties in computed self-diffusion coefficients of around three orders of magnitude across a wide span of temperatures and oxygen partial pressures, demonstrating that direct connections between computation and experiment are now increasingly possible.

Conflicts of interest

There are no conflicts to declare.

Acknowledgements

This work is supported by the U.S. National Science Foundation under grants DMR 13-06822 and DMR 17-09327. Computational resources were provided by the Illinois Campus Cluster and the Blue Waters sustained-petascale computing project, which is supported by the National Science Foundation (awards OCI-0725070 and ACI-1238993) and the state of Illinois. Blue Waters is a joint effort of the University of Illinois at Urbana-Champaign and its National Center for Supercomputing Applications.

References

1 P. Gorai, E. Ertekin and E. G. Seebauer, *Appl. Phys. Lett.*, 2016, **108**, 241603.
2 A. G. Hollister, P. Gorai and E. G. Seebauer, *Appl. Phys. Lett.*, 2013, **102**, 231601.
3 E. G. Seebauer, K. Dev, M. Y. L. Jung, R. Vaidyanathan, C. T. M. Kwok, J. W. Ager, E. E. Haller and R. D. Braatz, *Phys. Rev. Lett.*, 2006, **97**, 55503.
4 C. Freysoldt, B. Grabowski, T. Hickel, J. Neugebauer, G. Kresse, A. Janotti and C. G. Van de Walle, *Rev. Mod. Phys.*, 2014, **86**, 253.
5 Y. Gao, Y. Liang and S. A. Chambers, *Surf. Sci.*, 1996, **365**, 638.
6 J. A. Rodriguez, T. Jirsak, G. Liu, J. Hrbek, J. Dvorak and A. Maiti, *J. Am. Chem. Soc.*, 2001, **123**, 9597.
7 J. A. Rodriguez, G. Liu, T. Jirsak, J. Hrbek, Z. Chang, J. Dvorak and A. Maiti, *J. Am. Chem. Soc.*, 2002, **124**, 5242.
8 M. Batzill, *Energy Environ. Sci.*, 2011, **4**, 3275.
9 T. Close, G. Tulsyan, C. A. Diaz, S. J. Weinstein and C. Richter, *Nat. Nanotechnol.*, 2015, **10**, 418.
10 M. Arita, M. Hosoya, M. Kobayashi and M. Someno, *J. Am. Ceram. Soc.*, 1979, **62**, 443.
11 F. Millot and C. Picard, *Solid State Ionics*, 1988, **28**, 1344.
12 H. Peng, *Phys. Lett. A*, 2008, **372**, 1527.
13 H.-Y. Lee, S. J. Clark and J. Robertson, *Phys. Rev. B: Condens. Matter Mater. Phys.*, 2012, **86**, 75209.
14 P. Gorai, A. G. Hollister, K. Pangan-Okimoto and E. G. Seebauer, *Appl. Phys. Lett.*, 2014, **104**, 191602.
15 K. M. Pangan-Okimoto, P. Gorai, A. G. Hollister and E. G. Seebauer, *J. Phys. Chem. C*, 2015, **119**, 9955.
16 K. L. Gilliard-AbdulAziz and E. G. Seebauer, *Phys. Chem. Chem. Phys.*, 2018, **20**, 4587.
17 L. Tsetseris, *Phys. Rev. B: Condens. Matter Mater. Phys.*, 2011, **84**, 165201.
18 B. P. Uberuaga and X.-M. Bai, *J. Phys.: Condens. Matter*, 2011, **23**, 435004.
19 J. A. Van Vechten and C. D. Thurmond, *Phys. Rev. B: Condens. Matter Mater. Phys.*, 1976, **14**, 3539.
20 M. Lannoo and G. Allan, *Phys. Rev. B: Condens. Matter Mater. Phys.*, 1982, **25**, 4089.
21 J. A. Van Vechten, *Phys. Rev. B: Condens. Matter Mater. Phys.*, 1986, **33**, 8785.
22 V. Kosyak, N. B. Mortazavi Amiri, A. V. Postnikov and M. A. Scarpulla, *J. Appl. Phys.*, 2013, **114**, 124501.
23 G. Roma, Y. Limoge and S. Baroni, *Phys. Rev. Lett.*, 2001, **86**, 4564.
24 P. Erhart and K. Albe, *Phys. Rev. B: Condens. Matter Mater. Phys.*, 2006, **73**, 115207.
25 R. W. Keyes, *J. Chem. Phys.*, 1958, **29**, 467.
26 F. Béjina, O. Jaoul and R. C. Liebermann, *Phys. Earth Planet. Inter.*, 2003, **139**, 3.
27 P. Hohenberg and W. Kohn, *Phys. Rev.*, 1964, **136**, B864.
28 W. Kohn and L. J. Sham, *Phys. Rev.*, 1965, **140**, A1133.
29 G. Kresse and J. Furthmüller, *Comput. Mater. Sci.*, 1996, **6**, 15.
30 G. Kresse and J. Furthmüller, *Phys. Rev. B: Condens. Matter Mater. Phys.*, 1996, **54**, 11169.
31 G. Kresse and D. Joubert, *Phys. Rev. B: Condens. Matter Mater. Phys.*, 1999, **59**, 1758.
32 J. P. Perdew, K. Burke and M. Ernzerhof, *Phys. Rev. Lett.*, 1996, **77**, 3865.
33 H. Perron, C. Domain, J. Roques, R. Drot, E. Simoni and H. Catalette, *Theor. Chem. Acc.*, 2007, **117**, 565.
34 P. M. Kowalski, B. Meyer and D. Marx, *Phys. Rev. B: Condens. Matter Mater. Phys.*, 2009, **79**, 115410.
35 J. K. Burdett, T. Hughbanks, G. J. Miller, J. W. Richardson Jr. and J. V. Smith, *J. Am. Chem. Soc.*, 1987, **109**, 3639.
36 G. Henkelman, B. P. Uberuaga and H. Jónsson, *J. Chem. Phys.*, 2000, **113**, 9901.
37 S. B. Zhang and J. E. Northrup, *Phys. Rev. Lett.*, 1991, **67**, 2339.
38 C. Freysoldt, J. Neugebauer and C. G. Van de Walle, *Phys. Status Solidi B*, 2011, **248**, 1067.
39 A. Von Hippel, J. Kalnajs and W. B. Westphal, *J. Phys. Chem. Solids*, 1962, **23**, 779IN1797.
40 J. Yahia, *Phys. Rev.*, 1963, **130**, 1711.
41 J. F. Baumard and E. Tani, *Phys. Status Solidi A*, 1977, **39**, 373.
42 R. H. Bube, *Photoconductivity of Solids*, R E Krieger, Pub. Co., 1966.
43 J. Pascual, J. Camassel and H. Mathieu, *Phys. Rev. B: Condens. Matter Mater. Phys.*, 1978, **18**, 5606.
44 V. P. Gupta and N. M. Ravindra, *J. Phys. Chem. Solids*, 1980, **41**, 591.
45 J. Nowotny, M. Radecka and M. Rekas, *J. Phys. Chem. Solids*, 1997, **58**, 927.
46 T. Bak, J. Nowotny and M. K. Nowotny, *J. Phys. Chem. B*, 2006, **110**, 21560.
47 C. T. M. Kwok, K. Dev, R. D. Braatz and E. G. Seebauer, *J. Appl. Phys.*, 2005, **98**, 13524.
48 E. G. Seebauer and M. C. Kratzer, *Charged Semiconductor Defects: Structure, Thermodynamics and Diffusion*, Springer Science & Business Media, 2008.
49 R. G. Breckenridge and W. R. Hosler, *Phys. Rev.*, 1953, **91**, 793.
50 H. P. R. Frederikse, *J. Appl. Phys.*, 1961, **32**, 2211.
51 W. R. Thurber and A. J. H. Mante, *Phys. Rev.*, 1965, **139**, A1655.

52 G. A. Acket and J. Volger, *Physica*, 1966, **32**, 1680.
53 J.-F. Baumard and F. Gervais, *Phys. Rev. B: Condens. Matter Mater. Phys.*, 1977, **15**, 2316.
54 V. Cristea and V. Babeş, *Phys. Status Solidi A*, 1978, **45**, 617.
55 J. W. DeFord and O. W. Johnson, *J. Appl. Phys.*, 1983, **54**, 889.
56 C. Kormann, D. W. Bahnemann and M. R. Hoffmann, *J. Phys. Chem.*, 1988, **92**, 5196.
57 E. Yagi, R. R. Hasiguti and M. Aono, *Phys. Rev. B: Condens. Matter Mater. Phys.*, 1996, **54**, 7945.
58 E. Hendry, F. Wang, J. Shan, T. F. Heinz and M. Bonn, *Phys. Rev. B: Condens. Matter Mater. Phys.*, 2004, **69**, 81101.
59 E. Rauls and T. Frauenheim, *Phys. Rev. B: Condens. Matter Mater. Phys.*, 2004, **69**, 155213.
60 B. Butorac and A. Mainwood, *Diamond Relat. Mater.*, 2008, **17**, 1225.
61 A. Togo and I. Tanaka, *Scr. Mater.*, 2015, **108**, 1.
62 Y. Mishin, M. R. Sørensen and A. F. Voter, *Philos. Mag. A*, 2001, **81**, 2591.
63 P. Ágoston and K. Albe, *Phys. Chem. Chem. Phys.*, 2009, **11**, 3226.
64 H. Kamisaka and K. Yamashita, *J. Phys. Chem. C*, 2011, **115**, 8265.
65 T. Brudevoll, E. A. Kotomin and N. E. Christensen, *Phys. Rev. B: Condens. Matter Mater. Phys.*, 1996, **53**, 7731.
66 P. Erhart, A. Klein and K. Albe, *Phys. Rev. B: Condens. Matter Mater. Phys.*, 2005, **72**, 85213.
67 A. Kushima, D. Parfitt, A. Chroneos, B. Yildiz, J. A. Kilner and R. W. Grimes, *Phys. Chem. Chem. Phys.*, 2011, **13**, 2242.
68 H. Bracht, *MRS Bull.*, 2000, **25**, 22.
69 S. Na-Phattalung, M. F. Smith, K. Kim, M.-H. Du, S.-H. Wei, S. B. Zhang and S. Limpijumnong, *Phys. Rev. B: Condens. Matter Mater. Phys.*, 2006, **73**, 125205.
70 H. Kamisaka, T. Hitosugi, T. Suenaga, T. Hasegawa and K. Yamashita, *J. Chem. Phys.*, 2009, **131**, 34702.
71 C. Zener, *J. Appl. Phys.*, 1951, **22**, 372.
72 E. Finazzi, C. Di Valentin, G. Pacchioni and A. Selloni, *J. Chem. Phys.*, 2008, **129**, 154113.
73 A. Janotti, J. B. Varley, P. Rinke, N. Umezawa, G. Kresse and C. G. Van, de Walle, *Phys. Rev. B: Condens. Matter Mater. Phys.*, 2010, **81**, 85212.
74 C. Ravi, C. Wolverton and V. Ozoliņš, *EPL*, 2006, **73**, 719.
75 M. Mantina, Y. Wang, R. Arroyave, L. Q. Chen, Z. K. Liu and C. Wolverton, *Phys. Rev. Lett.*, 2008, **100**, 215901.
76 G. Lucas and R. Schäublin, *Nucl. Instrum. Methods Phys. Res., Sect. B*, 2009, **267**, 3009.
77 K. Schmalzl, D. Strauch and H. Schober, *Phys. Rev. B: Condens. Matter Mater. Phys.*, 2003, **68**, 144301.
78 P. Srepusharawoot and U. Pinsook, *Phys. Status Solidi B*, 2005, **242**, 1598.
79 P. Thibaudeau, A. Debernardi, V. T. Phuoc, S. Da Rocha and F. Gervais, *Phys. Rev. B: Condens. Matter Mater. Phys.*, 2006, **73**, 64305.
80 J. W. L. Pang, W. J. L. Buyers, A. Chernatynskiy, M. D. Lumsden, B. C. Larson and S. R. Phillpot, *Phys. Rev. Lett.*, 2013, **110**, 157401.
81 U. Kürpick, A. Kara and T. S. Rahman, *Phys. Rev. Lett.*, 1997, **78**, 1086.
82 K. L. Gilliard and E. G. Seebauer, *J. Phys.: Condens. Matter*, 2017, **29**, 445002.
83 M. Li and E. G. Seebauer, *J. Phys. Chem. C*, 2018, **122**, 2127.
84 C. V. Phillips, *Epidemiol.*, 2003, **14**, 459.
85 C. Steinbrink and S. Lehnhoff, *EUROCON 2015-International Conference on Computer as a Tool (EUROCON), IEEE*, 2015, pp. 1–6.